**Jens Nørkær Sørensen**
Associate Professor,
Department of Mechanical Engineering,
Building 403,
Technical University of Denmark,
DK-2800 Lyngby,
Denmark

**Wen Zhong Shen**
Associate Professor,
Department of Mechanical Engineering,
Building 403,
Technical University of Denmark;
Associate Professor,
Research Center for High Speed Trains,
Changsha Railway University,
China

# Numerical Modeling of Wind Turbine Wakes

*An aerodynamical model for studying three-dimensional flow fields about wind turbine rotors is presented. The developed algorithm combines a three-dimensional Navier-Stokes solver with a so-called actuator line technique in which the loading is distributed along lines representing the blade forces. The loading is determined iteratively using a blade-element approach and tabulated airfoil data. Computations are carried out for a 500 kW Nordtank wind turbine equipped with three LM19.1 blades. The computed power production is found to be in good agreement with measurements. The computations give detailed information about basic features of wind turbine wakes, including distributions of interference factors and vortex structures. The model serves in particular to analyze and verify the validity of the basic assumptions employed in the simple engineering models.*
[DOI: 10.1115/1.1471361]

## 1 Introduction

Load and performance calculations of wind turbines are today routinely performed by the Blade-Element/Momentum (BEM) method (Glaubert [1]). This method is based on dividing the flow in annular control volumes and applying momentum balance and energy conservation in each control volume. The annuli are bounded by stream surfaces that enclose the rotor and extend from far upstream to far downstream. Basic assumptions of the method are that the induced velocity in the rotor plane is equal to one half of the induced velocity in the ultimate wake, and that the flow can be analyzed by dividing the blade into a number of independent elements. For each blade element the aerodynamic forces are obtained using tabulated airfoil data, derived from wind tunnel measurements and corrected for three-dimensional effects. Because the BEM model is simple and very fast to run on a computer, it has gained an enormous popularity and is today the only design code in use by industry. However, owing to limitations of representing all the various flow situations encountered in practice, it has become necessary to introduce different empirical corrections. Such situations include phenomena related to dynamic inflow, yaw misalignment, tip loss and heavily loaded rotors. There exists thus an increasing need to establish experiments and to develop more advanced models to evaluate the basic assumptions underlying the BEM model. Although there today seems to be no realistic alternative that may replace the BEM model as an industrial design tool, more advanced inviscid models have been developed to overcome the limitations of the momentum approach.

One such method is the vortex wake method. In this method the shed vorticity in the wake is employed to compute the induced velocity field. The vorticity may either be distributed as vortex line elements (Miller [2], Simoes and Graham [3], and Bareiss et al. [4]) or as discrete vortices (Voutsinas et al. [5]), with vortex distributions determined either as a prescribed wake or a free wake. A free wake analysis may in principle provide one with all relevant informations needed to understand the physics of the wake. However, this method can be very computing demanding and tends to diverge owing to the intrinsic singularities of vortex lines.

Another method is the asymptotic acceleration potential method (van Holten [6] and van Bussel [7]). This method is based on solving a Poisson equation for the pressure, assuming small perturbations of the mean flow. Compared to vortex wake models, the

method is fast to run on a computer. The model has been used to analyze various flow cases, such as dynamic inflow and yawed flow. The main limitation of the model is that it is based on linearized flow equations, hence further development of the technique is required when analyzing flows about rotors subject to high loadings.

Finally, yet another class of inviscid methods is the generalized actuator disk method. This type of model represents a straightforward extension of the BEM model, as it employs tabulated airfoil data along with the conservation laws. The main difference is that the annular independence of the BEM model is replaced by the solution of a full set of Euler or Navier-Stokes equations. Axisymmetric versions of the method have been developed and solved either by analytical/semi-analytical methods (Wu [8], Greenberg [9], Conway [10,11]) or by finite difference/finite volume methods (Sørensen and Myken [12], Sørensen and Kock [13], Madsen [14]). In helicopter aerodynamics similar approaches have been applied by e.g., Fejtek and Roberts [15] who solved the flow about a helicopter employing a chimera grid technique in which the rotor was modelled as an actuator disk, and Rajagopalan and Mathur [16] who modelled a helicopter rotor using time-averaged momentum source terms in the momentum equations. Comparisons with experiments have demonstrated that the method works well for axisymmetric flow conditions and can provide usefull informations regarding phenomena such as dynamic inflow (Sørensen and Kock [13]) and turbulent wake states occurring for heavily loaded rotors (Sørensen et al. [17]). The main limitation of the method is that the forces are distributed evenly along the actuator disk, hence the influence of the blades is taken as an integrated quantity in the azimuthal direction.

To avoid the problem of using corrected or calibrated airfoil data various hybrid viscous/inviscid models have been developed. Sørensen [18] used a quasi-simultaneous interaction technique to study the influence of rotation on the stall characteristics of a wind turbine rotor. Sankar and co-workers (Berkman et al. [19]) developed a hybrid Navier-Stokes/full-potential/free wake method for predicting three-dimensional unsteady viscous flows over isolated helicopter rotors in hover and forward flight. The method has recently been extended to cope with horizontal axis wind turbines (Xu and Sankar [20]). Another hybrid method is due to Hansen et al. [21] who combined a three-dimensional Navier-Stokes solver with an axisymmetric actuator disk model.

Recently, full three-dimensional computations employing the Reynolds-averaged Navier-Stokes (RaNS) equations have been carried out by Ekaterinaris [22], Duque et al. [23], and Sørensen and Michelsen [24]. Although the RaNS methods are able of cap-

turing the pre-stall behavior, because of inaccurare turbulence modelling and grid resolution RaNS methods still fail to capture correctly the stall behavior.

To overcome the limitations of the axisymmetric actuator disk model, we here present a new model that combines a three-dimensional Navier-Stokes solver with a technique in which body forces are distributed radially along each of the rotor blades. Thus, the kinematics of the wake is determined by a full three-dimensional Navier-Stokes simulation whereas the influence of the rotating blades on the flow field is included using tabulated airfoil data to represent the loading on each blade. Although a Navier-Stokes solver is employed for studying the global flow field, the flow of interest is essentially inviscid, and viscous effects from the boundary layer are introduced only as integrated quantities through the use of airfoil data. The airfoil data and subsequent loading are determined iteratively by computing local angles of attack from the movement of the blades and the local flow field. The technique we refer to as the actuator line concept. The concept enables us to study in detail the dynamics of the wake and the tip vortices and their influence on the induced velocities in the rotor plane. The main motivation for developing such a model is to analyze and verify the validity of the basic assumptions that are employed in the simpler more practical engineering models.

In Section 2 the mathematical model and the computation algorithm are described. Section 3 describes how the body forces are derived from local blade-element considerations employing tabulated airfoil data. In section 4 numerical results are presented for the flow past a Nordtank 500/41 wind turbine equipped with three LM19.1 blades. First, to validate the code, comparisons between numerical results and experimental data are provided and a study on grid sensitivity is carried out. Good agreement with the measured power curve is found. Next, global flow fields about the rotor are analyzed. Distributions of induced velocities in the rotor plane as well as the structure of the wake are computed. Particularly, it is shown that the model is capable of predicting distinct tip vortices and their location in the wake.

## 2 Mathematical Model and Numerics

The flow model combines the actuator line concept with a finite difference discretization of the Navier-Stokes equations. The equations are formulated in vorticity-velocity ($\boldsymbol{\omega}-\mathbf{V}$) variables and solved in a cylindrical coordinate system ($r$, $\theta$, $z$). The formulation, which is obtained by applying the curl operator on the Navier-Stokes equations in primitive variables (i.e., velocity-pressure) consists of three transport equations for the vorticity components, three definition equations connecting velocity and vorticity, and the continuity equation, as shown below,

$$\frac{\partial \boldsymbol{\omega}}{\partial t} + \nabla \times (\boldsymbol{\omega} \times \mathbf{V}) = -\nu \nabla \times (\nabla \times \boldsymbol{\omega}) + \nabla \times \mathbf{f}_\epsilon, \qquad (1)$$

$$\nabla \times \mathbf{V} = \boldsymbol{\omega}, \quad \nabla \cdot \mathbf{V} = 0, \qquad (2)$$

where $\nu$ is the kinematic viscosity and $\mathbf{f}_\epsilon$ is the loading which is introduced as a body force on the right-hand side of the momentum equations.

When solving Eqs. (1) and (2), continuity is automatically ensured, hence the problem of the pressure-velocity coupling associated with a primitive variables formulation is avoided. The vorticity formulation, on the other hand, is complicated by the additional constraint that the vorticity field has to be solenoidal as well. Furthermore, the scalar representation of Eq. (2) constitutes a set of 4 equations in 3 unknowns and, therefore, comprises an over-determined system that calls for special solution techniques. In Huang and Ghia [25] it was demonstrated that a unique solution of the system is possible provided that the velocity boundary conditions satisfy the constraint of zero mass flow out of the boundaries. In the present work a least-squares method is employed to solve Eq. (2).
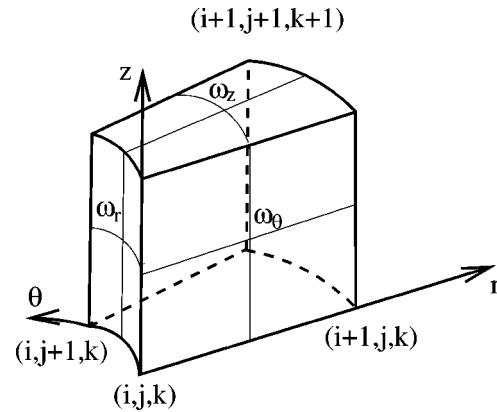


**Fig. 1  Staggered grid arrangement**

In principle, a solenoidal vorticity field is obtained by writing the transport equations in rotational form. It is important, however, that the discretization in itself does not introduce any artificial production terms due to truncation errors. This problem is solved by employing a staggered grid in which the vorticity components are defined at the face centers of the computational boxes. Thus, denoting by ($r_i, \theta_j, z_k$) the coordinates to the lower left corner point of a computational box, $\omega_r$ is located at ($r_i, \theta_{j+1/2}, z_{k+1/2}$), $\omega_\theta$ is located at ($r_{i+1/2}, \theta_j, z_{k+1/2}$), $\omega_z$ is located at ($r_{i+1/2}, \theta_{j+1/2}, z_k$), and the corresponding transport equations are discretized about the same locations. The staggered grid arrangement is shown in Fig. 1.

Time integration is performed by utilizing a Crank-Nicolson type scheme for the diffusive terms and an explicit Adams-Bashforth discretization of the convection and stretching terms. Employing a notation in which $\mathbf{L}_d$ denotes the diffusive terms and $\mathbf{L}_c$ the convective and stretching terms, Eq. (1) may in short be written as

$$\frac{\partial \boldsymbol{\omega}}{\partial t} - \mathbf{L}_d(\boldsymbol{\omega}) = \mathbf{L}_c(\boldsymbol{\omega}) + \nabla \times \mathbf{f}_\epsilon, \qquad (3)$$

which in discretized form reads

$$\frac{2}{\Delta t} \boldsymbol{\omega}^{n+1} - \mathbf{L}_d^{n+1}(\boldsymbol{\omega}) = \frac{2}{\Delta t} \boldsymbol{\omega}^n + \mathbf{L}_d^n(\boldsymbol{\omega}) + 3\mathbf{L}_c^n(\boldsymbol{\omega})$$
$$- \mathbf{L}_c^{n-1}(\boldsymbol{\omega}) + 2\nabla \times \mathbf{f}_\epsilon^n, \qquad (4)$$

where $\Delta t$ is the time step and superscript 'n' refers to the time at which the operator is evaluated. The spatial discretization is carried out employing central differences for the diffusive terms and the force terms, and the second order upwinding scheme QUICK for the remaining terms. The resulting set of coupled difference equations is solved simultaneously for all vorticity components by an iterative line-relaxation method.

After having advanced the vorticity in time, the velocity field is updated by solving the Cauchy-Riemann equations, Eq. (2), with the newly calculated vorticity on the right-hand side. These equations constitute a set of four first order differential equations. To avoid wiggles from odd-even decoupling the equations are discretized by use of a box scheme. As we are seeking the solution for only three variables, i.e., the velocity components ($V_r, V_\theta, V_z$), the system is overdetermined and the solution is accomplished by employing a least-squares method. This is found by applying the conjugate gradient method on the associated normal equations. In discretized form, Eq. (2) is expressed as:

$$\underline{\underline{A}}\, \underline{V} = \underline{b}, \qquad (5)$$

where $\underline{\underline{A}}$ is a $m \times q$ coefficient matrix, $\underline{V}$ is a vector containing $q$ unknown velocity components and the right-hand vector $\underline{b}$ con-
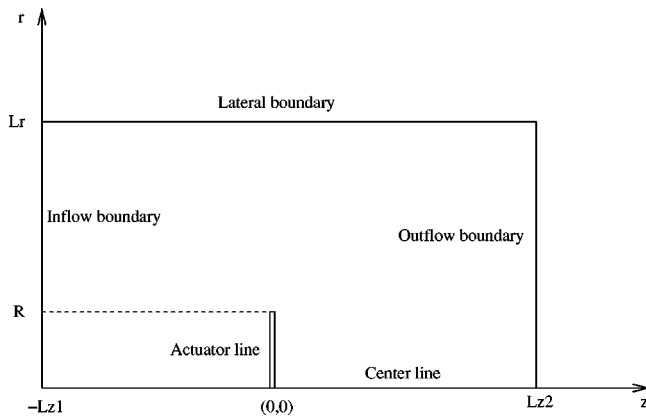
**Fig. 2   Cross section of computational domain**

tains $m$ elements. This system is overdetermined and solved using an iterative least squares method. This is accomplished by replacing Eq. (5) by its normal system

$$(\underline{A}^T\underline{D}\underline{D}\underline{A})\underline{V}=\underline{A}^T\underline{D}\underline{D}\underline{b}, \tag{6}$$

where $\underline{D}$ is a diagonal matrix introduced for the purpose of scaling. The elements on the diagonal of $\underline{D}$ are $d_{ii}=\|a_i\|_2$, where $a_i$ denotes the $i$th row of $\underline{A}$. This choice of $\underline{D}$ weights all equations equally. It may be noted that solving Eq. (6) is equivalent to minimize the functional

$$I=\frac{1}{2}\int\int\int_v[(\nabla\cdot\mathbf{V})^2+\|\nabla\times\mathbf{V}-\boldsymbol{\omega}\|^2]dv. \tag{7}$$

The solution of Eq. (6) is found by applying a standard conjugate gradient method. Further details about the solution algorithm can be found in Shen and Ta Phuoc [26] and Sørensen et al. [27].

The computational domain is limited by $r\in[0,L_R]$, $\theta\in[0,2\pi/3]$ and $z\in[-L_{z1},L_{z2}]$, where $L_R$ denotes the radius to the lateral boundary, $L_{z1}$ and $L_{z2}$ denote the distances to the upstream and the downstream boundary, respectively, and $\theta$ is the azimuthal angle defined positive counter-clockwise. The computational domain is shown in Fig. 2. To reduce the computing time the calculations are carried out in a domain comprising one third of the rotor area by imposing periodicity in the azimuthal direction.

To close the equations, boundary conditions are introduced as follows. At the inflow boundary a constant axial wind velocity is specified. At the outflow boundary downstream the rotor a Neumann condition is imposed for the axial velocity component. At the lateral boundary the radial velocity is put equal to zero. Boundary conditions for the vorticity are everywhere established from the vorticity definition equations. To summarize, the boundary conditions for velocity and vorticity are defined as follows:

Lateral boundary ($r=L_R,0\leq\theta\leq2\pi/3,-L_{z1}\leq z\leq L_{z2}$):

$$V_r=0, \quad \omega_\theta=-\frac{\partial V_z}{\partial r}, \quad \omega_z=\frac{1}{r}\frac{\partial(rV_\theta)}{\partial r}.$$

Inflow boundary ($0\leq r\leq L_R,0\leq\theta\leq2\pi/3,z=-L_{z1}$):

$$V_z=V_o, \quad \omega_r=-\frac{\partial V_\theta}{\partial z}, \quad \omega_\theta=\frac{\partial V_r}{\partial z}.$$

Outflow boundary ($0\leq r\leq L_R,0\leq\theta\leq2\pi/3,z=L_{z2}$):

$$\frac{\partial V_z}{\partial z}=0, \quad \omega_r=\frac{1}{r}\frac{\partial V_z}{\partial\theta}, \quad \omega_\theta=-\frac{\partial V_z}{\partial r}.$$

The boundary conditions are imposed such that the velocity conditions are used in the Cauchy-Riemann system, Eq. (2), and the vorticity conditions are employed in the transport equations, Eq.

(1). As the transport equations are written in curl-form, no boundary conditions are necessary for the solution of the $\omega_z$-transport equation at in-and outflow boundaries.

In principle, the flow is inviscid, but in order to stabilize the solution diffusive terms are retained. Thus, an effective Reynolds number is defined as $\mathrm{Re}=V_oR/\nu$, where $R$ is the radius of the rotor and $V_o$ is the undisturbed velocity. It is important to note that the Reynolds number only has a limited influence on the flow behavior, as vorticity is only produced along the lines representing the rotor blades and subsequently convected and diffused away from these. The vorticity sources are introduced into the equations through the body forces appearing on the right-hand side of Eq. (1). It is known from flows past bluff bodies that the drag coefficient and the essential flow behavior do not depend on the Reynolds number, provided that it has reached a certain minimum value (Sørensen et al. [17]).

## 3   Determination of Body Forces

To determine the body forces acting on the rotor blades we use a blade-element approach combined with two-dimensional airfoil characteristics. In Fig. 3, a cross-sectional element at radius $r$ defines the airfoil in the $(\theta,z)$ plane. Denoting the tangential and axial velocity in the inertial frame of reference as $V_\theta$ and $V_z$, respectively, the local velocity relative to the rotating blade is given as

$$\mathbf{U}_{\mathrm{rel}}=(V_\theta-\Omega r,V_z). \tag{8}$$

The angle of attack is defined as

$$\alpha=\phi-\gamma, \tag{9}$$

where $\phi=\tan^{-1}(V_z/(\Omega r-V_\theta))$ is the angle between $\mathbf{U}_{rel}$ and the rotor plane and $\gamma$ is the local pitch angle. The force per spanwise unit length is

$$\mathbf{f}_{2D}=\frac{d\mathbf{F}}{dr}=\frac{1}{2}\rho U_{\mathrm{rel}}^2c(C_L\mathbf{e}_L+C_D\mathbf{e}_D), \tag{10}$$

where $C_L=C_L(\alpha,\mathrm{Re})$ and $C_D=C_D(\alpha,\mathrm{Re})$ are the lift and drag coefficients, respectively, $c$ is the chord length, and $\mathbf{e}_L$ and $\mathbf{e}_D$ denote the unit vectors in the directions of the lift and the drag, respectively. The lift and drag coefficients are determined from measured or computed two-dimensional airfoil data that are corrected for three-dimensional effects. There are several reasons why it is necessary to correct the airfoil data. First, at separation rotational effects limit the growth of the boundary layer, resulting in an increased lift as compared to two-dimensional characteristics. Various correction formulas for rotational effects have been derived using quasi three-dimensional approaches (see e.g., Snel
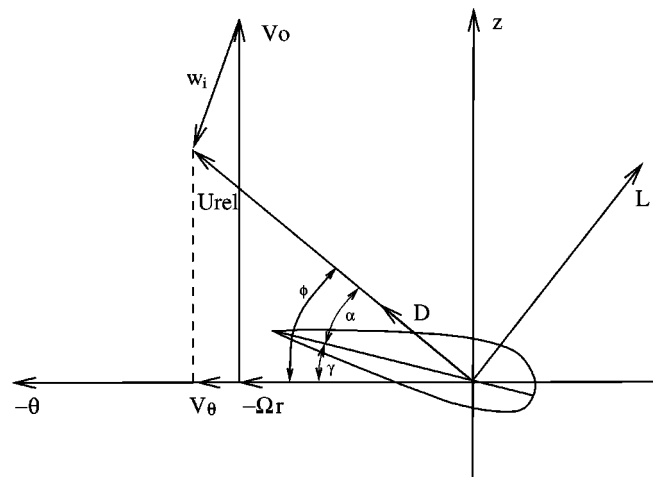


**Fig. 3   Cross-sectional airfoil element**

et al. [28] and Chaviaropoulos and Hansen [29]). Next, the airfoil characteristics depend on the aspect ratio of the blade. This is in particular pronounced at high incidences where the finite aspect ratio drag coefficient, $C_D$, is much smaller than the corresponding one for an infinite blade. As an example, for a flat plate at an incidence $\alpha = 90$ deg the drag coefficient $C_D = 2$ for an infinitely long plate, whereas for aspect ratios corresponding to the geometry of a wind turbine blade $C_D$ takes values in the range 1.2–1.3. In Hoerner [30] it is stated that the normal force from a flat plate is approximately constant for 45 deg $< \alpha <$ 135 deg, indicating that in this range both $C_L$ and $C_D$ have to be reduced equally. Hansen [31] proposes to reduce $C_L$ and $C_D$ by an expression that takes values in range from 0.6–1.0, depending on the ratio between the distance to the tip and the local chord length. It should be noticed, however, that this is only a crude guideline and that most airfoil data for wind turbine use is calibrated against actual performance and load measurements. This also explains why most manufacturers of wind turbine blades are reluctant to change well-tested airfoil families.

Considering an element of differential size, $dv = r\,dr\,d\theta\,dz$, the force is given by

$$\mathbf{f} = \frac{d\mathbf{F}}{dv} = \frac{\mathbf{f}_{2D}}{r\,d\theta\,dz}. \tag{11}$$

Projecting this vector on the coordinate directions we get

$$f_r = 0, \tag{12}$$

$$f_\theta = \frac{\rho c U_{rel}^2}{2 r\,d\theta\,dz}(C_L \sin\phi - C_D \cos\phi), \tag{13}$$

$$f_z = \frac{\rho c U_{rel}^2}{2 r\,d\theta\,dz}(C_L \sin\phi + C_D \cos\phi). \tag{14}$$

The kinematics of the flow may also be expressed in terms of the induced velocity,

$$w_i = (-aV_o, -a'\Omega r), \tag{15}$$

where the axial flow interference factor is defined as

$$a = 1 - \frac{V_z}{V_o}, \tag{16}$$

and the tangential flow interference factor

$$a' = -\frac{V_\theta}{\Omega r}. \tag{17}$$

As the source term in Eq. (1) is given as the curl of the load, it acts as a singular vorticity source along the rotor blades. To avoid singular behavior, $\mathbf{f}_\epsilon$ is formed by taking the convolution of the computed normal load, $\mathbf{f}$, and a regularization kernel, $\eta_\epsilon$, as shown below

$$\mathbf{f}_\epsilon = \mathbf{f} \otimes \eta_\epsilon,$$

where

$$\eta_\epsilon(r) = \frac{1}{\epsilon^3 \pi^{3/2}} \exp[-(r/\epsilon)^2].$$

Here $\epsilon$ is a constant that serves to adjust the strength of the regularization function and $r$ is the distance between the measured point and the initial force points on the rotor. In the case of three blades, the regularized force becomes

$$\mathbf{f}_\epsilon(\mathbf{x}) = \sum_{i=1}^{3} \int_0^R \mathbf{f}_{2D}(r)\,\eta_\epsilon(|\mathbf{x} - r\mathbf{e}_i|)\,dr,$$

where $\mathbf{e}_i$ denotes the unit vector of the blade direction. Denoting the position of the first blade in cylindrical coordinates by $(r, \theta_o, z_o)$, the two other positions are given as $(r, \theta_o + 2\pi/3, z_o)$ and $(r, \theta_o + 4\pi/3, z_o)$, respectively. The reason for introducing the

function $\eta_\epsilon$ is to distribute smoothly the loading on more than one mesh point. The influence of the parameter $\epsilon$ has been studied in Sørensen et al. [17].

## 4 Results and Discussion

We here compute the global flow field past a 500 kW Nordtank wind turbine equipped with three LM19.1 blades. The turbine has a rotor diameter of 41 m and runs at a tip speed $V_{tip} = 58$ m/s. The blade sections consist of NACA 63-4xx series airfoils on the outer 8 m of the blade and of FFA-W3-xxx airfoils on the remaining inner part. The blade has approximately a linear chord distribution from $r = 4.5$ m to $r = 18.0$ m and is twisted gradually from 0 at the tip to 20 deg at $r = 4.5$ m. The chord and thickness distributions range from about 1.6 m and 53% at $r = 4.5$ m to about 0.1 m and 15% at $r = 20.5$ m, respectively. The airfoil data is based on two-dimensional measurements up to and just beyond stall (see Abbott and Doenhoff [32] and Björck [33]).

For higher incidences, no data are available for these profiles and instead data for NACA 0012 and Göttingen 420 were employed (Riegels [34]). The data were furthermore corrected for three-dimensional effects, as described in Section 3. The data were tabulated at four spanwise stations for incidences ranging from $\alpha = -10$ to $\alpha = 110$ deg. Adaptation to the computational mesh was accomplished by using linear interpolation. The data were kindly provided by Øye (private communication) and are normally used for BEM calculations in the Flex5 aeroelastic code. They were not modified in the present work.

The computations are carried out in a domain in which the inflow and the outflow boundary is located 20 rotor-radii, respectively, upstream and downstream of the rotor. The radial extent of the domain comprises 10 rotor-radii measured from the rotational axis. To capture the gradients of the flow field, grid points are concentrated near the blade tips and stretched in radial as well as in axial direction. The resulting grid consists of 100 grid points in the radial direction, 99 points in the axial direction and 50 points in the azimuthal direction. The mesh is equidistant in the $\theta$-direction, i.e., $\Delta\theta = 0.044$. In the axial direction the grid spacing ranges from $\Delta z = 0.036$ at the rotor plane to about $\Delta z = 1.6$ in the far wake, and in the radial direction the spacing takes values from $\Delta r = 0.022$ near the tip to about $\Delta r = 0.4$ at the lateral boundary. The computations are carried out at an effective Reynolds number of 5000. As discussed earlier, using a low Reynolds number does not have an effect on the flow behavior at the blades, but will cause the wake to become more diffusive. The grid spacing and the value of the used Reynolds number is of course a compromise between accuracy and computing costs.

**4.1 Validation of Numerical Model.** To validate the numerical model the power yield of the Nordtank wind turbine was computed and compared to measurements. The comparison is shown in Fig. 4 that displays the mechanical power as a function of wind speed. For wind speeds up to about $V_0 = 12$ m/s excellent agreement is found between computed and measured values. At high wind speeds, however, the mechanical power is overpredicted with up to about 5%. This discrepancy is most probably related to inaccurate airfoil data as the induced velocities are almost negligible at high wind speeds. For $V_0$ greater than 12 m/s the rotor is stalled, and most of the flow on the suction side of the blade is separated. Hence, the airfoil data are subject to severe three-dimensional effects and become less reliable.

To quantify the influence of the employed grid, a computation on a finer mesh consisting of $150 \times 50 \times 148$ points was carried out for $V_0 = 10$ m/s. Comparisons of the force distributions computed by use of the two grids are shown in Fig. 5. Any difference between the two computations are barely seen and we conclude that the original grid is sufficiently fine to ensure accurate solutions.

To ensure that the flow is fully developed in most of the wake we let the computations run to about $t = 20$. With a timestep of $\Delta t = 2 \cdot 10^{-3}$ this corresponds to a total of about $10^4$ time steps.
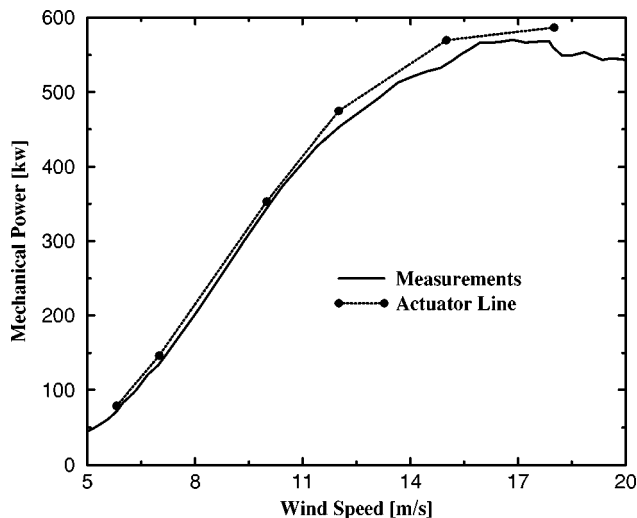
**Fig. 4 Comparison of measured and computed mechanical power production for the Nordtank 500/41 wind turbine**



**Fig. 6 Computed vorticity field showing the formation of the wake structure at $V_o = 10$ m/s**

**4.2 Wake Structures.** In the following we show some representative numerical results that characterize the wake structure of the rotor. The results shown are computed at a wind speed $V_0 = 10$ m/s, corresponding to a tip speed ratio of 5.8. Figure 6 depicts iso-vorticity contours illustrating the downstream development of the wake vortices. The bound vorticity of the blades is seen to be shed downstream from the rotor in individual vortex tubes. These vortices persist about 2 turns after which they diffuse into a continuous vortex sheet. From experiments it is known that distinct spiral structures are maintained more turns than what is depicted in Fig. 6. It is most likely the combined effect from the low Reynolds number and the somewhat coarse grid downstream of the rotor that causes a too early diffusion of the vortex tubes.

Figure 7 shows the distribution of the axial interference factor, Eq. (16), in the rotor plane. The three blades are seen as lines with a high density of iso-lines, owing to the large changes in induced velocity that takes place across the blades. The number of iso-lines is 30 and the value between two successive lines is equidistant. The values range from $-0.15-0.55$, with peak values appearing near the mid-section of the blades (with a positive value on

one side of the blade and a negative value on the other). The tip vortices appear as localized regions with negative $a$-values, with a minimum of about $-0.11$, corresponding to an axial velocity that is 11% higher than the inflow wind speed.

Following $a$ in the azimuthal direction at a constant radius (see Fig. 8), the distribution is seen to be dominated by rather high minimum and maximum values. For the case treated here we compute values of $a$ going from 0.55 on one side of the blade to $-0.10$ on the other side of the blade, with the mean value located about halfway between two blades. The dramatic jump in $a$ is due to the induction from the bound vorticity located on the blade. To compare the interference factors $a$ and $a'$, defined in Eqs. (16) and (17), with results from BEM or axisymmetric actuator disk models, we compute averaged values from the formulas
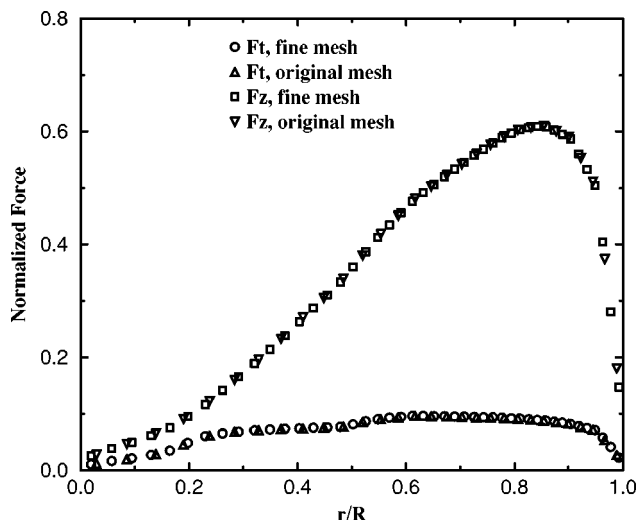


**Fig. 5 Comparison of force distributions computed on the original mesh ($100 \times 50 \times 99$) and on the fine mesh ($150 \times 50 \times 148$) at $V_o = 10$ m/s**
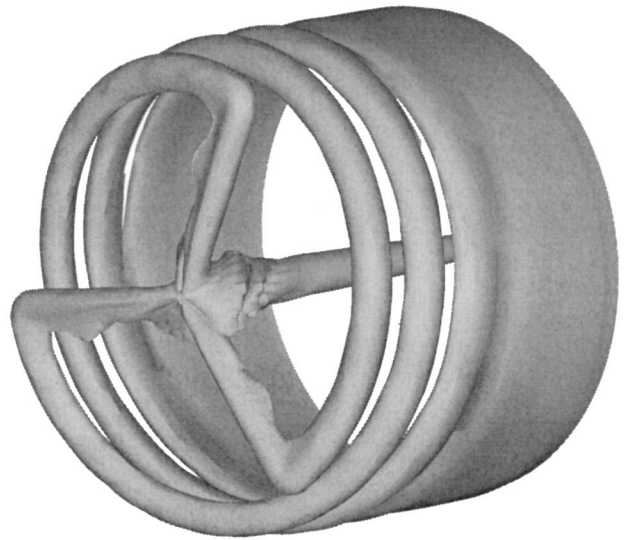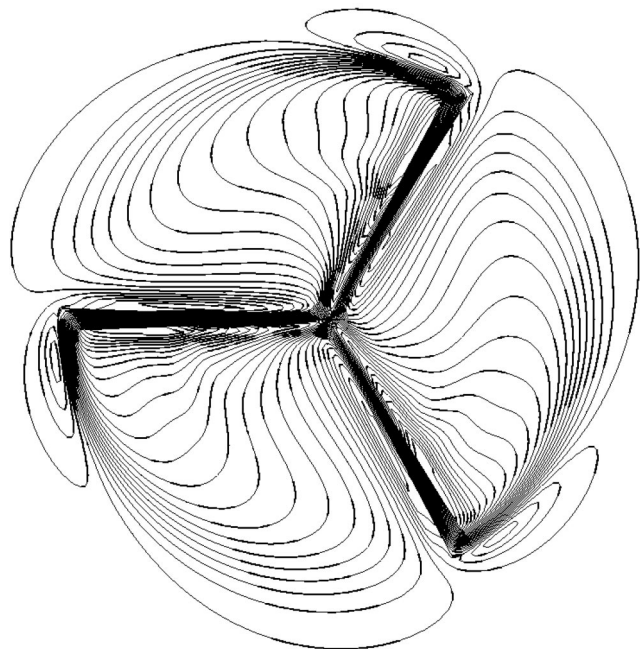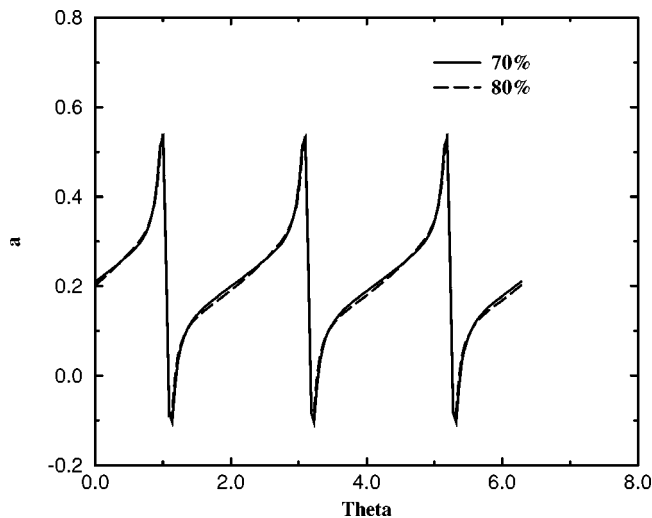


**Fig. 7 Distribution of axial interference factor, $a = 1 - Vz/Vo$, in the rotor plane at $V_o = 10$ m/s**

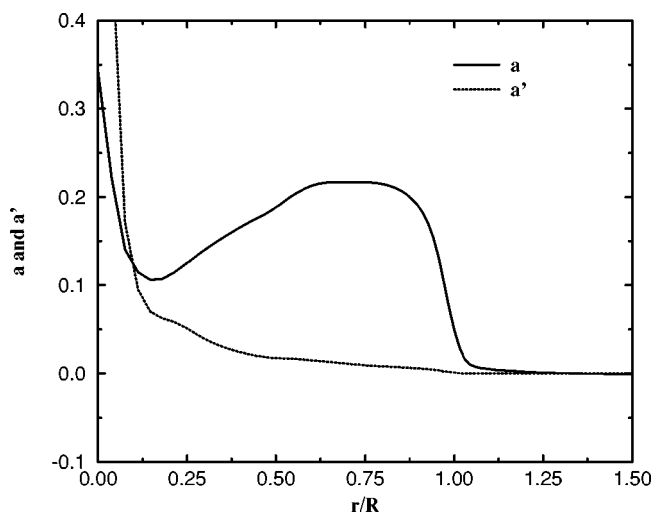**Fig. 8 Azimuthal distribution of axial interference factor, a, at $V_o=10$ m/s. Solid line: Distribution along $r=70\%R$; Dashed line: Distribution along $r=80\%R$**
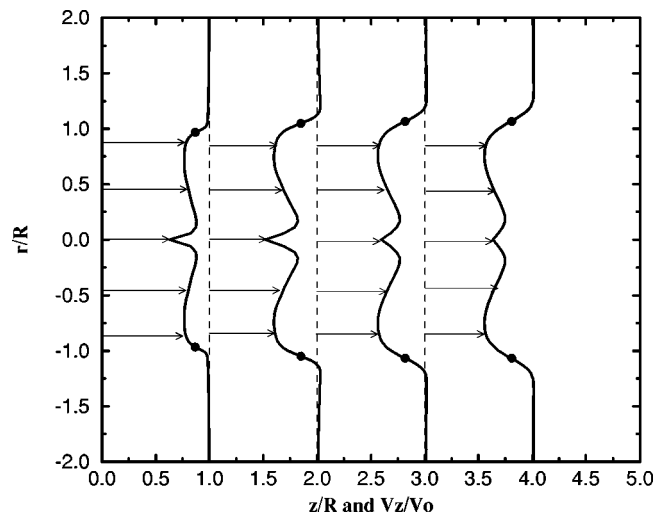


**Fig. 10 Distribution of axial velocity for $V_o=10$ m/s. The core of the tip vortices are marked by ●**

$$\bar{a}(r) = \frac{1}{2\pi} \int_0^{2\pi} a(r,\theta)d\theta, \quad \overline{a'}(r) = \frac{1}{2\pi} \int_0^{2\pi} a'(r,\theta)d\theta.$$

$$(18)$$

Figure 9 depicts the radial distributions of $\bar{a}$ and $\overline{a'}$. It is seen that $\overline{a'}$ decreases monotonously from a value of 0.4 at $r/R=0.05$ to zero at the tip. In contrast to the smooth behavior of $\overline{a'}$, $\bar{a}$ exhibits local maxima at both $r=0$ and at $r/R=0.75$. Both interference factors exhibit values in the order of 0.1, showing that the induced velocities at $V_0=10$ m/s has a relatively large influence on the performance and the loading of the rotor.

The development of the axial velocity distribution in the wake is depicted in Fig. 10. The velocity distributions are averaged in the azimuthal direction and plotted at axial positions $z/R=0$, 1, 2, and 3. Outside the wake the value of the axial velocity attains the one of the undisturbed wind. A small overshoot is observed at $z/R=2$. For all velocity profiles a distinct minimum occurs at $r=0$. This is caused by the loading on the inner part of the blade

that is dominated by large drag forces. The position of the tip vortices (see also Fig. 6) is inferred as dots on the velocity profiles. As can be seen they are generally located midway between the wake and the external flow at the position where the gradient of the axial velocity attains its maximum value.

## 5 Conclusion

A numerical model for predicting global flow fields about rotors of wind turbines was presented. The model is based on a so-called actuator line concept in which the blade loading, implemented along lines representing the rotor blades, is introduced in the Navier-Stokes equations as body forces.

The model was validated against experiments of a three-bladed 500 kW Nordtank wind turbine. The computed power distribution was found to be in good agreement with experimental results.

The computations demonstrated that the global flow field about the rotor is well represented by letting the loading on the blades be determined by body forces distributed along lines. In the near wake the shed vortices appeared as distinct vortex tubes, although they after about 2 turns are diffused into a continuous vortex sheet.

Useful informations about the structure of the flow field behind the rotor were obtained. In particular, the axial interference factor in the rotor plane and the position of the tip vortices in the immediate wake behind the rotor were analyzed in details.

An important future application of the model will be to analyze the validity of the assumptions underlying simpler practical engineering models, such as the blade-element momentum method. In particular, future applications of the model are planned to focus on tip corrections, curved or tapered blade shapes and yaw misalignment.

**Fig. 9 Radial distributions of averaged interference factors $\bar{a}(r)$ and $\overline{a'}(r)$, defined in Eqs. (16)–(18), computed at $V_o=10$ m/s**

## References

[1] Glauert, H., 1963, "Airplane Propellers," *Aerodynamic Theory*, Durand, W. F., ed., Dover, New York.
[2] Miller, R. H., 1983, "The Aerodynamic and Dynamic Analysis of Horizontal Axis Wind Turbines," J. Wind. Eng. Ind. Aerodyn., **15**, pp. 329–340.
[3] Simoes, F. J., and Graham, J. M. R., 1991, "Prediction of Loading on a Horizontal Axis Wind Turbine using a Free Vortex Wake Model," Proc. 13th BWEA Wind Energy Conference, Quarton, D. C. and Fenton, V. C., eds., Mechanical Engineering Publications Limited, London, U.K., pp. 247–254.
[4] Bareiss, R., and Wagner, S., 1993, "A Hybrid Wake Model for HAWT," Proc.

of the Sixth IEA Symposium on the Aerodynamics of Wind Turbines, McAnulty, K. F., ed., ETSU, Harwell, pp. 7.1–7.10.

[5] Voutsinas, S. G., Beleiss, M. A., and Rados, K. G., 1995, ''Investigation of the Yawed Operation of Wind Turbines by Means of a Vortex Particle Method,'' AGARD Conf. Proc., **552**, pp. 11.1–11.11.

[6] van Holten, Th., 1975, ''The Computation of Aerodynamic Loads on Helicopter Blades in Forward Flight using the Method of the Acceleration Potential,'' Report VTH-189, Dept. of Aerospace Eng., Delft Univ. of Techn., The Netherlands.

[7] van Bussel, G. J. W., 1995, ''The Aerodynamics of Horizontal Axis Wind Turbine Rotors Explored with Asymptotic Expansion Methods,'' Doctoral dissertation, Technische Universiteit Delft, The Netherlands.

[8] Wu, T. Y., 1962, ''Flow Through a Heavily Loaded Actuator Disc,'' Schiffstechnik, **9**, pp. 134–138.

[9] Greenberg, M. D., 1972, ''Nonlinear Actuator Disc Theory,'' Z. Flugwiss., **20** (3), pp. 90–98.

[10] Conway, J., 1995, ''Analytical Solutions for the Actuator Disk with Variable Radial Distribution of Load,'' J. Fluid Mech., **297**, pp. 327–355.

[11] Conway, J., 1998, ''Exact Actuator Disk Solution for Non-uniform Heavy Loading and Slipstream Contraction,'' J. Fluid Mech., **365**, pp. 235–267.

[12] Sørensen, J. N., and Myken, A., 1992, ''Unsteady Actuator Disc Model for Horizontal Axis Wind Turbines,'' J. Wind. Eng. Ind. Aerodyn., **39**, pp. 139–149.

[13] Sørensen, J. N., and Kock, C. W., 1995, ''A model for Unsteady Rotor Aerodynamics,'' J. Wind. Eng. Ind. Aerodyn., **58**, pp. 259–275.

[14] Madsen, H. Aa., 1996, ''A CFD Analysis for the Actuator Disc Flow Compared with Momentum Theory Results,'' Proc. of the 10th IEA Symposium on the Aerodynamics of Wind Turbines, Pedersen, B. M., ed., Department of Fluid Mechanics, Technical University of Denmark, pp. 109–124.

[15] Fejtek, I., and Roberts, L., 1992, ''Navier-Stokes Computation of Wing/rotor Interaction for a Tilt Rotor in Hover,'' AIAA J., **30** (11), pp. 2595–2603.

[16] Rajagopalan, R. G., and Mathur, S. R., 1993, ''Three Dimensional Analysis of a Rotor in Forward Flight,'' J. Am. Helicopter Soc., **38** (3).

[17] Sørensen, J. N., Shen, W. Z., and Munduate, X., 1998, ''Analysis of Wake States by a Full-field Actuator Disc Model,'' Wind Energy, **1**, pp. 73–88.

[18] Sørensen, J. N., 1986, ''Three-level, Viscous-inviscid Interaction Technique for the Prediction of Separated Flow Past Rotating Wings,'' Ph.D. thesis, AFM Report 86-07, Department of Fluid Mechanics, The Technical University of Denmark.

[19] Berkman, M. E., Sankar, L. N., Berezin, C. R., and Torok, M. S., 1997, ''A Navier-Stokes/full potential/free wake Method for Rotor Flows,'' AIAA Paper 97-0401.

[20] Xu, G., and Sankar, L. N., 1999, ''Computational Study of Horizontal Axis Wind Turbines,'' AIAA Paper 99-0042.

[21] Hansen, M. O. L., Sørensen, J. N., Michelsen, J. A., and Sørensen, N. N., 1997, ''A Global Navier-Stokes Rotor Prediction Model,'' AIAA Paper 97-0970.

[22] Ekaterinaris, J. A., 1997, ''Numerical Simulation of Incompressible Two-bladed Rotor Flow Field,'' AIAA Paper 97-0398.

[23] Duque, E. P. N., van Dam, C. P., and Hughes, S., 1999, ''Navier-Stokes Simulations of the NREL Combined Experiment Phase II Rotor,'' AIAA Paper 99-0037.

[24] Sørensen, N. N., and Michelsen, J. A., 2000, ''Aerodynamic Predictions for the Unsteady Aerodynamics Experiment Phase-II Rotor at the National Renewable Energy Laboratory,'' AIAA Paper 2000–0037.

[25] Huang, Y., and Ghia, U., 1992, ''A Multigrid Method for Solution of Vorticity Velocity Form of 3-D Navier-Stokes Equations,'' Commun. Appl. Numer. Methods, **8** (10), pp. 707–719.

[26] Shen, W. Z., and Ta Phouc, L., 1997, ''Numerical Method for Unsteady 3D Navier-Stokes Equations in Velocity-vorticity Form,'' Comput. Fluids, **26**, pp. 93–216.

[27] Sørensen, J. N., Shen, W. Z., and Hansen, M. O. L., 2002, ''A Vorticity-velocity Formulation of the 3D Navier-Stokes Equations in Cylindrical Coordinates,'' Submitted.

[28] Snel, H., Houwink, R., and Piers, W. J., 1993, ''Sectional Prediction of 3D Effects for Separated Flow on Rotating Blades,'' Proc. of the ECWEC '93 Conference, pp. 395–399.

[29] Chaviaropoulos, P. K., and Hansen, M. O. L., 2000, ''Investigating Three-dimensional and Rotational Effects on Wind Turbine Blades by Means of a Quasi-3D Navier-Stokes Solver,'' ASME J. Fluids Eng., **197**, pp. 330–336.

[30] Hoerner, S. F., 1965, *Fluid-Dynamic Drag*, published by the author.

[31] Hansen, M. O. L., 1999, ''Polar for NACA 63-415 Airfoil,'' Report ET-AFM-9902, Department of Energy Engineering, Technical University of Denmark.

[32] Abbott, I. H., and Doenhoff, A. E., 1959, *Theory of Wing Sections*, Dover Publications, New York.

[33] Björck, A., 1996, ''A Guide to Data Files from Wind Tunnel Test of a FFA-W3-211 Airfoil at FFA,'' Technical Report FFA P-V-019, FFA, Bromma, Sweden.

[34] Riegels, F. W., 1961, *Aerofoil Sections*, Butterworths, London.